ITRF/LhARA Milestone M2.2 report

First SCAPA Ion Source Simulations and Experiments

Work Package 1.2

R.J. Gray[1,2], T.S. Dascalu[3], R. Wilson[1], T. Wilson[1], C.A.J. Palmer[4], N.P. Dover[5], P. McKenna [1]

[1] *Department of Physics, SUPA, University of Strathclyde, John Anderson Building, 107 Rottenrow East,Glasgow G4 0NG, UK*
[2] *Cockcroft Institute, Daresbury Laboratory, Sci-Tech Daresbury, Keckwick Ln, Daresbury, Warrington UK*
[3] *Department of Physics, Lancaster University, Bailrigg, Lancaster LA1 4YW, UK*
[4] *School of Mathematics and Physics, Queen's University Belfast, Belfast, BT7 1NN, UK*
[5] *John Adams Institute for Accelerator Science, Imperial College London, London SW7 2AZ, UK*

Abstract

Here we present the results of the first experiments performed on the SCAPA facility to optimise the proton source for the LhARA project serving the Ion Therapy Research Facility. We describe the key steps undertaken in order to optimise the laser and other key laboratory systems for ion acceleration at up to 1 Hz repetition rates. We then introduce measurements of the proton source performance, showing maximum proton energies exceeding 15 MeV and $\approx 10^9$ protons per shot in a band 10±1 MeV. We quantify the source stability and identify key parameters to further optimise the source performance for future radiobiology experiments. In addition we present a multiscale simulation study involving both particle-in-cell and hydrodynamic simulations which will support the design and development of future source experiments on SCAPA.

Contents

1 Introduction

WP1.2 aims to develop and test the technology required for the laser-driven ion source serving the Ion Therapy Research Facility (ITRF) ITRF. WP1.2 has successfully developed an active collaboration between all the major laser driven ion source groups in the UK, including the University of Strathclyde, Queen's University Belfast, Lancaster University, Imperial College London, and the Central Laser Facility. The collaboration is working effectively, with regular meetings and cross institute collaborative projects. The funding from the ITRF has enabled increased staff effort at the partner institutes, and is allowing us to make clear progress towards our project objectives.

In this milestone report, we will detail the first experiments performed using the bunker B area of Scottish Centre for the Application of Plasma Based Accelerators (SCAPA) and its 350 TW laser. The experimental work reported herein consists of a total access period of 7 weeks, split between July 2023 to July 2024 with periods of analysis and system development in between. Over the course of these experiments key underpinning methodologies needed for LhARA were tested and developed including a new data collection and control system, a 2D spatial-spectral proton beam profiler and a high-repetition rate analysis code for ion spectra. Alongside these developments we will report on the new understanding gained about the performance of the SCAPA laser and how it has been optimised for laser-driven ion experiments. Within this period we were successfully able to demonstrate a laser-driven proton source capable of operating at up to 1 Hz with a maximum energy of at least 15 MeV and $\approx 10^9$ protons per shot in a band 10 ± 1 MeV.

This experimental work was complimented by a programme of multi-scale simulations making use of both hydrodynamic modelling of the front surface expansion of the target and particle-in-cell modelling of the high-intensity laser-plasma interaction and resulting ion source. These simulations made use of experimental measurements of key laser and target properties made on SCAPA to reach close agreement between experiments and simulation.

This combined approach of an experimental and simulation programme sets the source development for LhARA in a strong position to deliver the required ion beam properties for future radiobiology experiments and to provide predictive modelling of potential laser-target configurations to aid in the design of the future ITRF.

2 Development of the SCAPA proton source

A series of related experiments were performed in the period July 2023 to July 2024 in order to optimise the laser-driven proton source in SCAPA and to develop methodologies required to characterise the proton source at repetition rates of up to 1 Hz. In the following subsections we will detail the development of the experimental setup in SCAPA and the performance of the 350 TW laser system (section 2.1), the optimisation and performance of the resulting proton source (section 2.3) and finally the measured stability of that source (section 2.4). We will also consider the current performance of the source in the context of its use for radiobiology experiments (section 2.5).

2.1 SCAPA beamline

The arrangement of the proton source beamline in SCAPA bunker B is shown in figure 1(a-c). The beamline consists of two separate vacuum chambers, one containing the plasma mirror system and the adaptive optic (AO) system to improve the temporal intensity contrast and the wavefront of the incoming laser pulse. The plasma mirror system was not used in any of the data reported here. These two vacuum chambers are shown

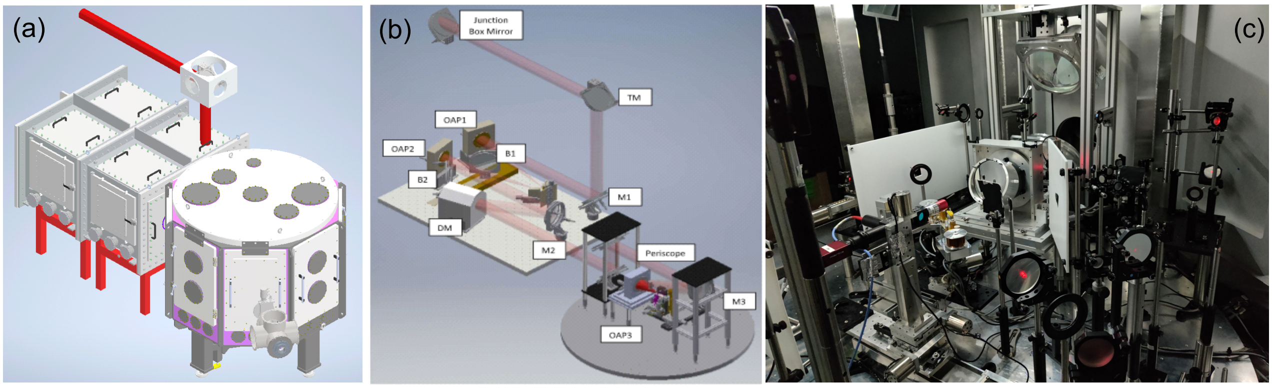

Figure 1: Images showing the setup of the bunker B beamline in SCAPA (a) CAD model of the plasma mirror and main vacuum chambers. (b) CAD model of the internal beamline layout (c) Photograph of the current experimental setup as used in the experiments detailed in this report.

as a CAD model in figure 1(a). Another view is shown in (b), indicating the beamline layout inside the plasma mirror chamber and the main interaction chamber. The beamline has a vertical, periscoped, arrangement where the laser pulse is directed to a higher level above the interaction before being turned back to the focusing F/1.5 off axis parabola (OAP). This design helps maximise the solid angle available in the horizontal plane around the target for diagnostic access. An image of this beamline layout and the experimental setup used for the data reported is shown in (c).

Alongside the construction of the beamline, dedicated effort was put into the development of the diagnostic systems required to monitor the proton source and complimentary diagnostic systems to monitor other aspects of the laser-plasma interaction. This includes the construction and installation of a Thomson Parabola (TP) ion spectrometer, a 2D proton beam profiler, focal-spot camera, optical probe and diagnostics to measure back scattered and reflected light in the chamber. Together this suite of systems enable detailed monitoring of both the laser-plasma interaction and the laser system performance.

In addition to the beamline layout and diagnostic development, a number of other key systems had to be developed as part of the source development. In order to operate the proton source at high repetition rates of up to 1 Hz, a tape target system was installed and the design iterated over the course of the first experiments. The version of the tape target system used in the collection of the data reported here is shown in figure 2(a-c). Shown in (a) is the full tape target system consisting of a reel of tape (here we use 13 μm kapton or 10 μm Steel tape) which is fed from one reel to another across a flat face plate. The face plate has a clear aperture in it and the laser irradiates the front surface of the tape, with the protons being accelerated from the rear surface and escaping through the clear aperture. An important insight made during the initial testing of the tape drive target in July 2023 was the difficulty in illuminating and aligning the target at the required angle of incidence (35°). This angle of incidence resulted in a clash (not initially expected but resulting from the tolerance of the CAD model) with the focal-spot camera. As a consequence, only indirect methods of target alignment were possible at that time (via alignment to a reference wire on top of the tape drive). This approach led to an unacceptable uncertainty on the target focal position. A number of changes were made to the design of the tape drive, which are illustrated in figure 2. The base plate of the tape target system was extended to make it wider, the tensioning arms of the drive were also moved further apart and the edges of the face plate were made with a larger angle chamfer. This combination of changes enabled the focal-spot camera system (which is used to align the target) to be driven close enough to the tape drive for it to be imaged directly, significantly improving the alignment accuracy. In addition to these changes, in order to make the tape target system more suitable for high-repetition rate experiments a trigger control signal was added so that the target is automatically replaced after being shot.

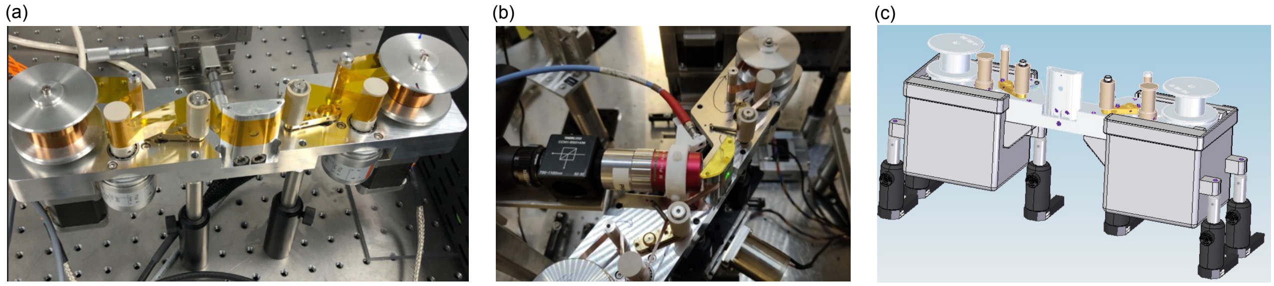

Figure 2: Images of the tape drive target developments (a) Image of the wider tape drive base to enable improved access for the focal-spot camera. (b) Updated target illumination setup (c) EMP shielding cages for the tape drive motors.

Modifications were also made to the focal-spot camera system, as shown in figure 2(b), where an infrared alignment diode was injected via a fibre optic placed at 35° to the target, such that the specular reflection is directed into the focal-spot objective. This development has significantly improved the target alignment quality and thus the accuracy of focusing. Figure 2(c) shows a further planned improvement to introduce shielding against electromagnetic pulses (EMP) for the tape target system by forming a Faraday cage around the main stepper motors. EMP has been observed as a ongoing issue which interupts the continous operation of the tape target system especially when metallic targets are used which, as we will show, also produced a higher energy proton source.

Another significant development during the first experiments on SCAPA for the proton source was on the development of new systems for data capture and analysis. This is an essential aspect of operating the proton source at 1 Hz in order to automatically control, stabilise and optimise key input parameters. Through the LPI-Py python library developed at Strathclyde, we have implemented an updated shot-control system. As shown in figure 3(a) this shot-control system enables the experimental team to define a parameter “scan file”. This scan file defines the parameters to be changed, the range over which they will be scanned and the number of points in that range. This enables multidimensional grid scans to be defined automatically. From the scan file the individual parameter values for a given shot are written into a “control file” which is then served to individual clients which control laboratory systems to change the laser energy, focusing, pulse duration and pre-heater parameters (as well as other system parameters as needed). The shot is then fired and the resulting data automatically transferred and processed by the in-built data analysis and database functionality of LPI-Py. This control system has also been designed to include machine-learning and optimisation algorithms. Currently a Bayesian optimisation algorithm is included to facilitate fast multidimensional optimisation by generating its own control files in order to maximise a given objective function. Also shown in figure 3(b) is an example image from a new dashboard system built via LPI-Py and the Grafana service. This dashboard system will enable a rapid and remote overview of the operation of the proton source in SCAPA.

2.2 Optimising the SCAPA laser performance for proton acceleration

During the first period of experiments at SCAPA significant time was spent characterising and improving the performance key parameters of the 350 TW laser in order to optimise conditions for laser-driven proton acceleration.

The laser pulse energy on target and the shot-to-shot stability of the laser energy is a key concern for the proton source. The laser pulse energy measured over N=197 repeat laser shots is shown in figure 4(a). The average laser pulse energy is found to be $\overline{E_L} = 6.0 \pm 0.1$ J. This laser pulse energy has a notable degree of

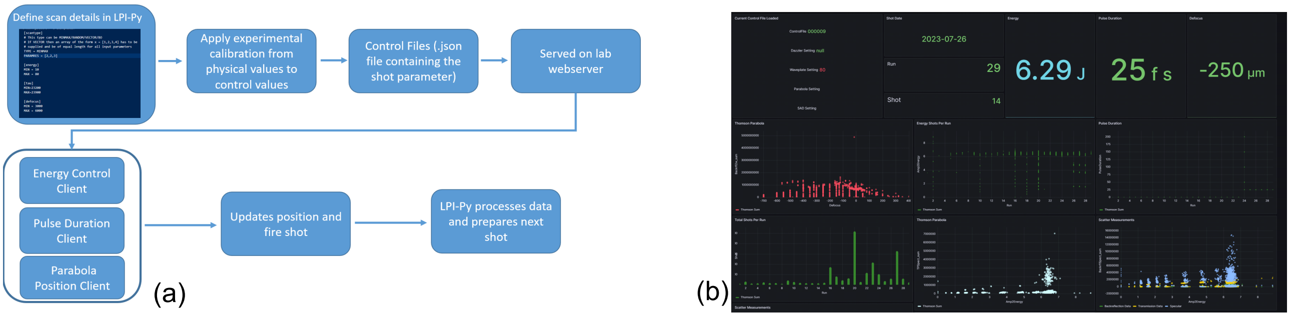

Figure 3: (a) Diagram of the automated data scan control capability. (b) Example image of the Grafana based dashboard system for monitoring source performance.

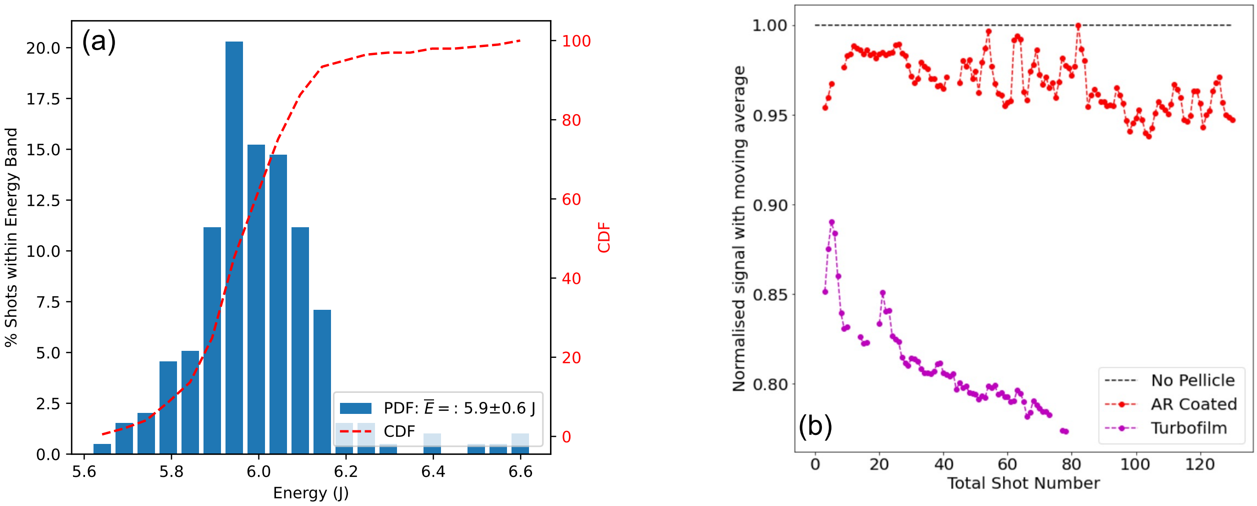

Figure 4: (a) Distribution of the laser energy as measured of N=197 repeat shots at full laser energy. (b) The measured transmission of the laser pulse through different pellicles as a function of shot number. The turbofilm (purple) is found to reduce in transmission much more quickly than the newer AR coated pellicles.

stability compared to similar laser systems of this type. The energy throughput of the laser was found to be 59% (energy before compressor is $\approx$10 J and energy on target is $\approx$6 J) via measurements with a calorimeter placed in the expanding beam after the OAP. This relatively high energy on target and good stability will support a good degree of shot-to-shot stability of the proton maximum energy and flux.

One of the key optics in the system that can affect laser energy on target is the protective pellicle (consisting of a <100 μm, transparent film) which is placed in front of the OAP in order to prevent debris produced from the laser interaction with the target damaging its surface. In the initial experiments in July 2023 we made use of a pellicle consisting of TurboFilm, a plastic monomer film used widely for optical protection in astronomy. As shown in figure 4(b), this material was found to burn rapidly and become damaged after tens of shots, attenuating the laser pulse by up to $\approx$ 25%. In January 2024 we undertook a series of tests comparing this pellicle with a new anti-reflection (AR) coated pellicle purchased from National Photocolor. Whereas the TurboFilm transmission drops by 15% over 80 shots (and is notably also attenuating the pulse without any damage from the first shot), the AR-coated pellicle starts close to 100% transmission and maintains that transmission within a 5% range over 120 shots. Subsequent measurements with targets in place have shown only minor additional damage forming on the pellicle after $>$ 1000 shots. These results indicate that the AR-

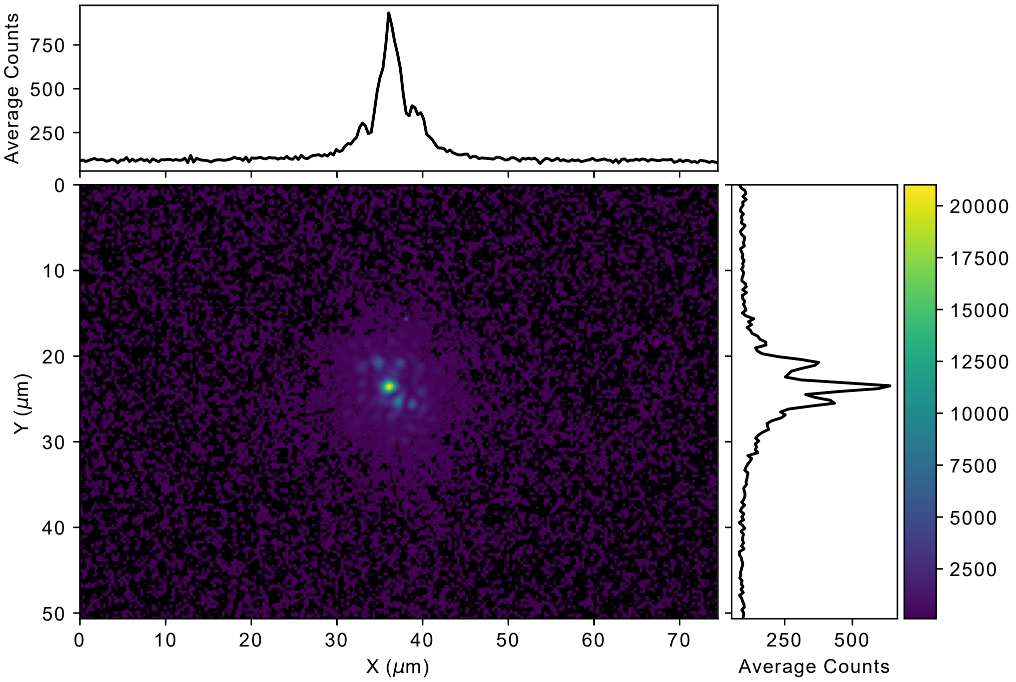

Figure 5: Example focal-spot image measured with a 20x microscope objective in SCAPA bunker B.

coated pellicles are sufficient for operations at full energy at 1 Hz for relatively sustained periods and are now sufficient for the requirements of the source-development phase of this project. However, it is important to also consider this as a key concern for long term operations. The replacement and monitoring of the pellicle will need to be designed in (as well as the significant associated costs) or alternative beamline configurations and targetry will need to be considered in the longer term to enable continuous > 1 Hz operations while mitigating debris issues.

In addition to the laser pulse energy on target another key laser-parameter in optimising the laser-driven proton source is the focal-spot size and encircled energy. An example focal-spot image from the F/1.5 OAP as measured by the focal-spot camera is shown in figure 5. Here the encircled energy of the spot is measured to be $\approx 20\%$ and the focal-spot size $\phi = 1.5\,\mu$m (FWHM). The focal-spot and encircled energy, combined with the measured energy throughput and pulse duration of the system enabled a peak laser intensity of $I_L = 1.4 \times 10^{21}$ W/cm^2 to be reached.

It is worth noting that it is possible to achieve higher quality focal-spots, which could more than double the encircled energy. The measured spot size is also approaching the resolution limit of the focal-spot camera system currently installed. Further work is planned for late 2024 to improve the quality of the focal-spot including the installation of a 50x microscope objective, an improved AO optimisation loop and a new OAP with a higher surface quality. This combined effort could help to more than double the number of protons in energy bands relevant for the radiobiology work that will come in the next phase, as well as increase the maximum proton energy.

Alongside the focal-spot size, it is important to consider the shot-to-shot spatial jitter of the focal-spot which may then induce variability in the pointing of the proton source and therefore poses challenges for capture beamline. This jitter can be caused by sources of vibration coupled into beamline optics or thermal expansion/contraction caused by temperature changes in the lab. The former leads to the focal-spot oscillating around a central position shot-to-shot and the later leads to a drift in the focal position over some period of time. We investigated both effects and saw no drift in the focal position over a period of 30 minutes. However we do

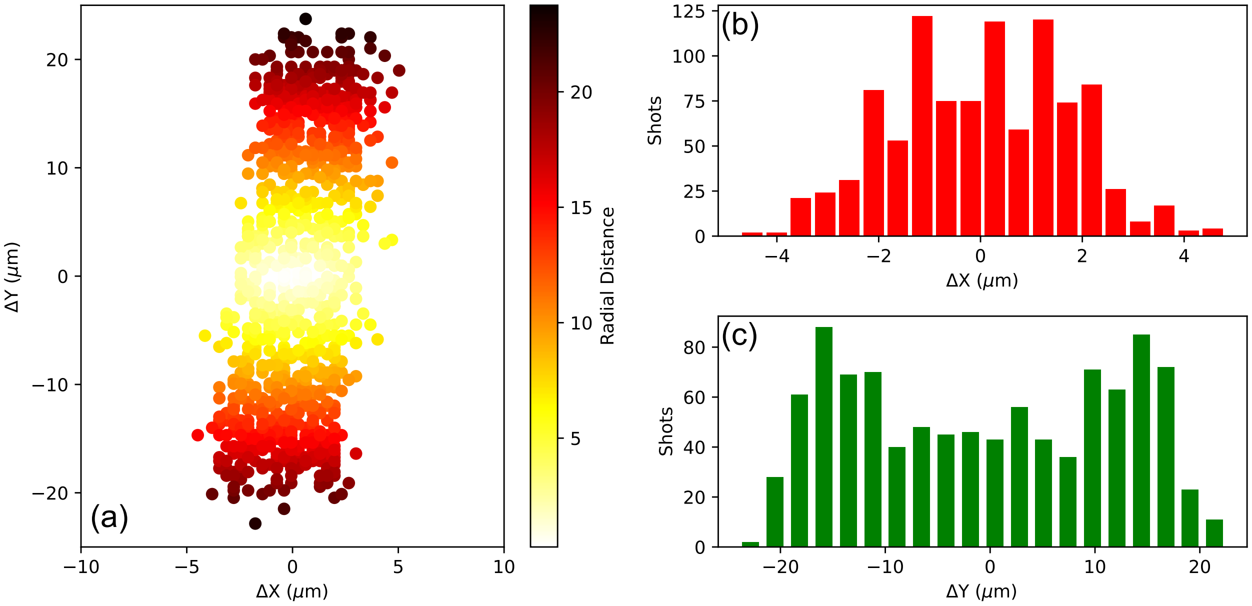

Figure 6: Measurements of the spatial jitter of the focal-spot over N=1000 shots. (a) The x- and y- displacement of the focal-spot position with the radial displacement from the center indicated on the colourbar. (b) Distribution of x-displacement (c) Distribution of the y-displacement.

see a relatively significant shot-to-shot jitter of the focal-spot in the Y-direction, as shown in figure 6(a). Here the centroid position of a focal-spot is measured for N=1000 pulses in a low power alignment mode. While the focal-spot varies around $\pm 4\,\mu$m in the x-direction, it varies $\pm 20\,\mu$m in the y-direction. Measuring the distribution of these points (shown in (b) and (c)), the jitter in the y-direction appears bimodal peaking around $\pm 15\,\mu$m. This suggests a positive and negative phase of oscillation of the spot induced by a source of vibration. Work on SCAPA has traced this source down to a single mirror after the compressor chamber in the laser area, a new mounting bracket will be installed to help to reduce this scale of this spatial jitter.

Another major aspect of the development work on the laser performance during these first experiments was a dedicated effort to improve the temporal intensity contrast. Early measurements of the temporal intensity contrast identified a series of prepulses in the trace (formed by post-pulse conversion to pre-pulses [1]). Although these prepulses were identified, it was not at the time clear if these were real prepulses or if they were introduced by the diagnostic measurement itself. It was also not clear if they were sufficient to cause meaningful expansion of the front surface of the target and result in a degradation of the resulting ion acceleration. After the first experiment, it was found that the maximum proton energies saturated at around 7 MeV for laser energy $E_L > 3$ J (well below the expected scaling from comparable systems). Modelling using the hydrodynamic FLASH code (some of which is detailed in section 3) also demonstrated that these prepulses were likely to be driving significant expansion of the front surface. To address this issue a series of tests were undertaken to identify the source of these prepulses and remove them. In most cases the source is the back reflection from the rear surface of a planar optic, such as a beam splitter or window. In case of SCAPA a number of the prepulses were identified as coming from the optics designed into the system for a separate probe arm which was not in use. These optics were removed and the large prepulses they induced were also removed. The resulting change in the temporal intensity contrast is shown in figure 7 as measured by a Tundra third order autocorrelator [2]. The data measured in January 2024 (where the maximum proton energy measured was only 7 MeV) show strong prepulses at -55 ps, -19 ps, -11 ps and -9.4 ps. Prepulses were also identified on longer timescales out

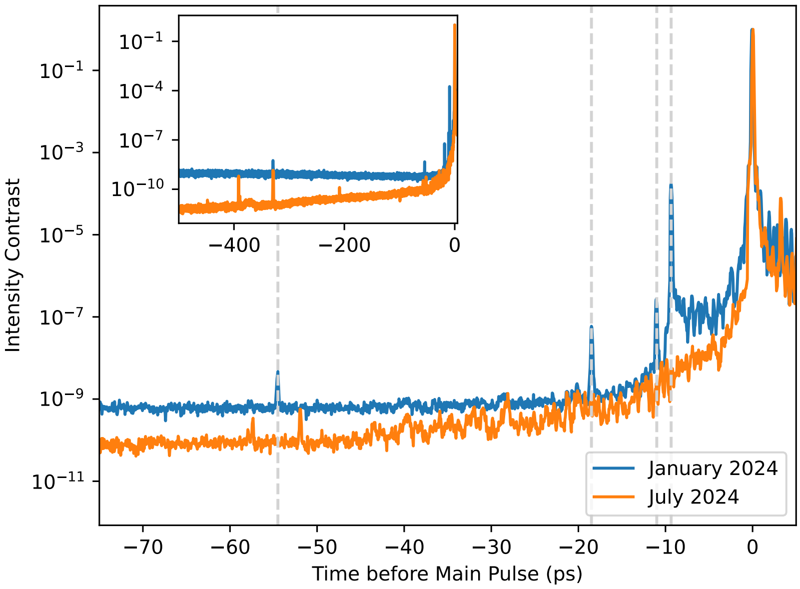

Figure 7: Example temporal intensity contrast measurement on SCAPA from January 2024 (blue) prior to work to remove prepulses in the system and from July 2024 (orange) after this work was completed. The inset figure shows the same data plotted on a over a longer time scale

to ≈ -400 ps (as shown in the inset figure) but, via hydrodynamic modelling with the FLASH code, these were found not to produce significant expansion. After removing optics from the beamline that were generating the prepulses the temporal intensity contrast was remeasured in July 2024, also shown in figure 7. Further work was also carried out to lower the noise floor of the Tundra, resulting in a more accurate measurement of the amplified spontaneous emission (ASE) pedestal on long timescales. From this measurement it is clear that the prepulses were successfully removed, the more accurate measurement of the ASE also revealed two low-intensity prepulses between -60 and -50 ps. These are not significant enough to produce expansion of the target front surface and are dominated by the effects of the pulse rising edge.

Further developments are possible to improve the temporal intensity contrast including reducing the rising edge of the pulse via reductions in the random phase noise introduced by optics in the compressor. Significantly larger improvements (up to 100x on the ps time scale) are also possible via the introduction and use of the double plasma mirror system. These developments would enable thinner targets to be used and potentially enable higher proton flux and maximum energy but would come at the cost of repetition rate and a lower energy on target. For radiobiology work that requires either single or few shot irradiations to achieve the required dose, this could be an optimal trade off. However working towards contrast improvements without plasma mirrors and towards suitably thin targets that can operate with the tape drive (or other target types such as liquid jet targets) provides the best route toward automation and high repetition rate operation of the source. At the present time, more work is required to establish exactly what preplasma conditions at the front of the target are needed to produce a more optimised source. It may be the case that the addition of a controlled prepulse or pulse shaping to introduce an ideal preplasma profile is required. This capability exists within SCAPA bunker B via the preheater beamline and the dazzler and will be the subject of further testing in late 2024.

The developments outlined above were a significant undertaking which have helped improved the overall performance of the SCAPA laser for laser-driven ion experiments in general and specifically for the require-

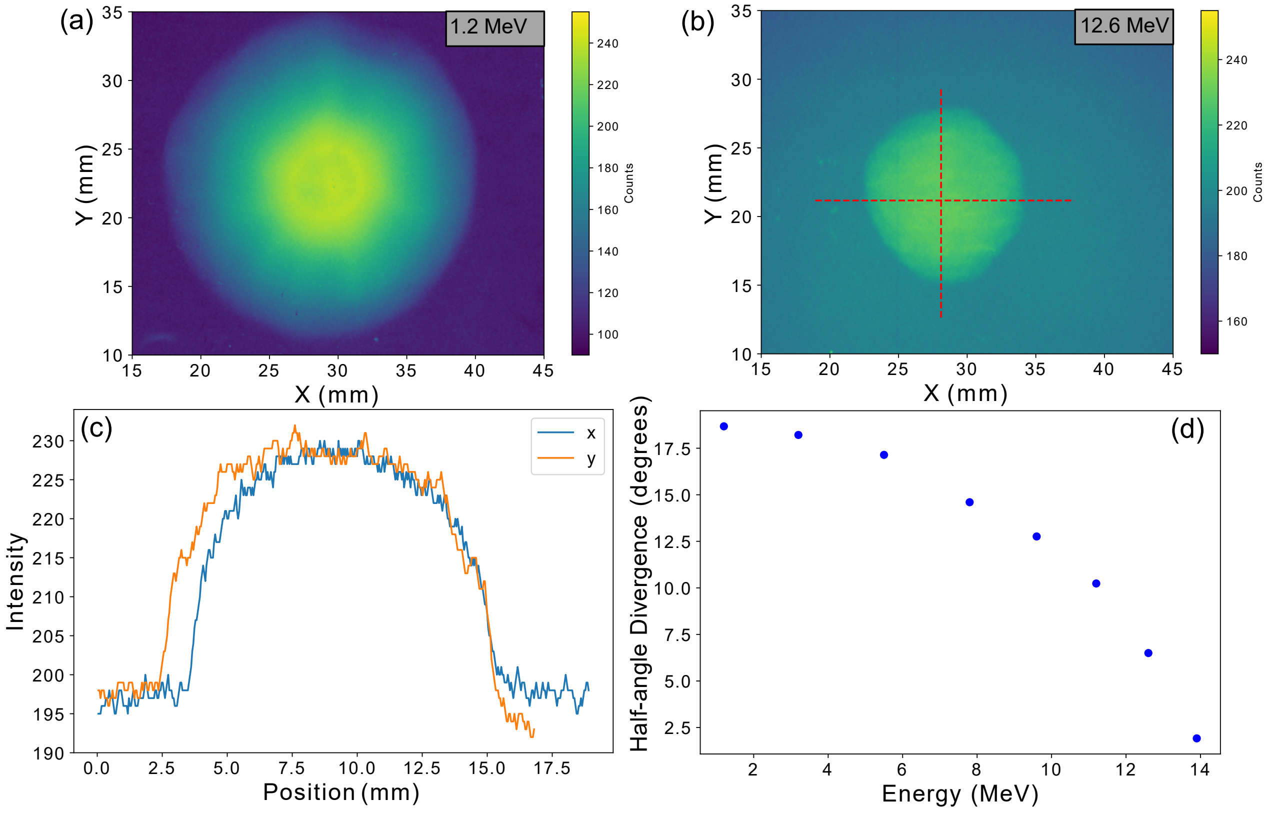

Figure 8: Example images of proton beam profile measured using RCF dosimetry stack. (a) Profile for 1.2 MeV protons measured on the first layer of RCF dosimetry stack. (b) Profile for 12.6 MeV protons measured on 7th layer of RCF dosimetry stack , also showing the region of the line out in X- and Y- (c) X- and Y- lineouts of the proton profile measured at 12.6 MeV. (d) Beam divergence as a function of proton energy.

ments of LhARA. In the next section we will detail the measured proton source performance under these laser conditions.

2.3 Proton source optimisation in SCAPA

After the contrast improvements were made as outlined above, a 3-week period of source development and testing was performed. All of the data reported in this section comes from that period of access unless otherwise stated. A number of initial data scans were performed by tuning the focal-spot size, pulse duration, laser energy, target material and target thickness in order to identify the conditions which produced the highest energy, highest flux proton source. A detailed scan was also performed with the preheater beamline to shape the front surface preplasma but no significant changes in the source were identified and it is likely that there was not sufficient delay between the preheater and the main pulse or not sufficient energy in this secondary beam (or both). Previous work has identified that optimisation along this dimension is likely to be beneficial, this will require further development on future experiments.

The optimal source performance was found for the highest laser energy (E=6.5 J), shortest pulse (τ =27 fs) and best focus ($\phi = 1.5\,\mu$m). Variation in the target material between kapton and steel also proved to be an important factor. Despite similar target thicknesses ($L_{Steel} = 10\,\mu$m and $L_{Kapton} = 13\,\mu$m) there is a $\approx 20\%$ increase in the maximum proton energy. A change in target thickness between kapton of $L = 25\,\mu$m

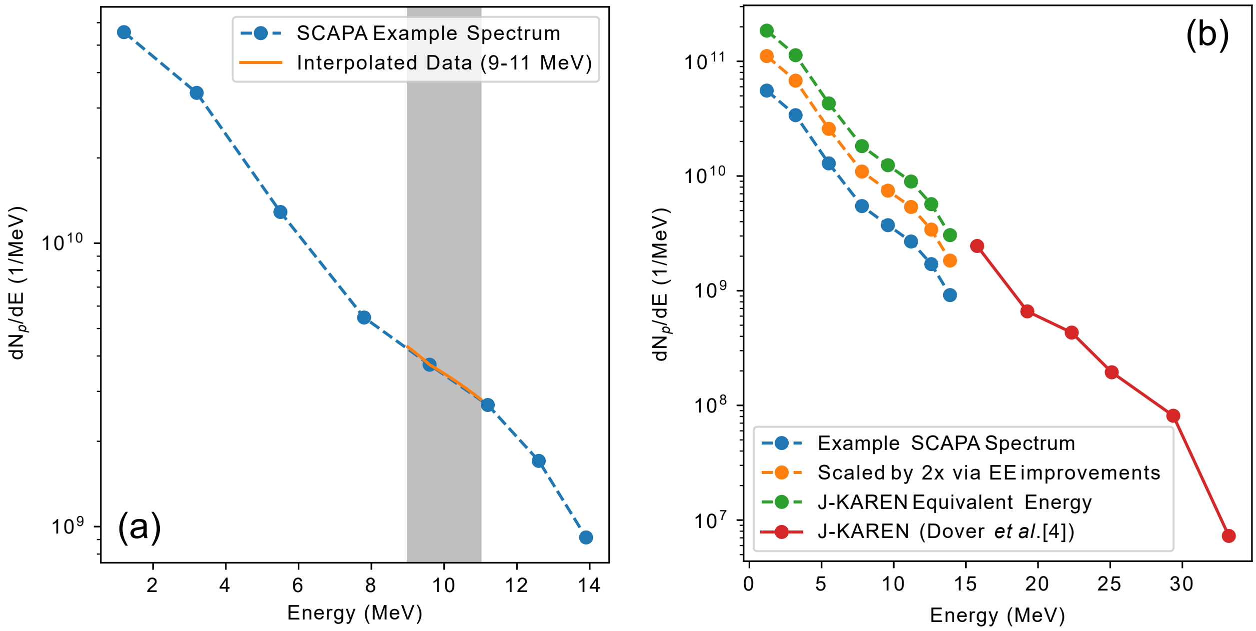

Figure 9: Example proton spectrum measured on RCF dosimetry stack (a) Proton spectrum shown in blue with grey box indicating 10 ± 1 MeV region relevant for use in radiobiology experiments. (b) Extrapolated spectra in comparison to previously published data from J-KAREN [5].

and $L = 13\,\mu$m did not produce a similar effect and therefore it is unlikely to be due to the difference in target thickness alone. It is likely that the different densities of target material result in a different degree of expansion of the front surface. FLASH modelling not shown here supports this conclusion, indicating that the steel target expands more than the kapton. This larger expansion can lead to improved coupling of laser energy into fast electrons which then drives the acceleration of the protons and also indicates the utility of using the preheater beam with the kapton tape on future experiments.

After these initial data scans to optimise the proton source a 50x50 mm Radiochromic Film (RCF) dosimetry stack was placed $d = 4.5$ cm from the rear surface of a $L = 10\,\mu$m steel tape target. From this measurement it is possible to produce a calibrated, spatially and spectrally resolved measurement of the proton beam. An example of the proton beam profile measured with this detector is shown in figure 8. Here the proton beam profile for the layer measuring 1.2 MeV protons is shown in (a) and the layer measuring 12.6 MeV protons is shown in (b). These beam profiles are notably different with the lower energy beam having a radial, ring like profile and the higher energy beam having a smooth flat-top profile. The ring like structure at low energies has been observed many times in laser-driven proton acceleration and is indicative of electron transport effects within the target, strong magnetic field formation at the rear surface or deformation of the rear surface [3, 4]. For radiobiology experiments relevant for LhARA we will be selecting out protons above $E_p = 10$ MeV, therefore this low energy structure will not dominate the dose deposition profile. In (c) we take a lineout through the middle of the beam shown in (b) in the x and y dimensions. This shows the beam profile is close to a parabolic profile with relative symmetry in the x and y dimensions. In (d) by measuring the extent of the beam as a function of depth within the RCF dosimetry stack we can calculate the beam divergence as a function of proton energy. This measurement shows the divergence monotonically decreasing with increasing energy. In the relevant band around 10 ± 1 MeV we find a divergence angle of $\approx 11^\circ$ half-angle. This relatively low angle of divergence will help support a high transmission into the beam capture system for LhARA.

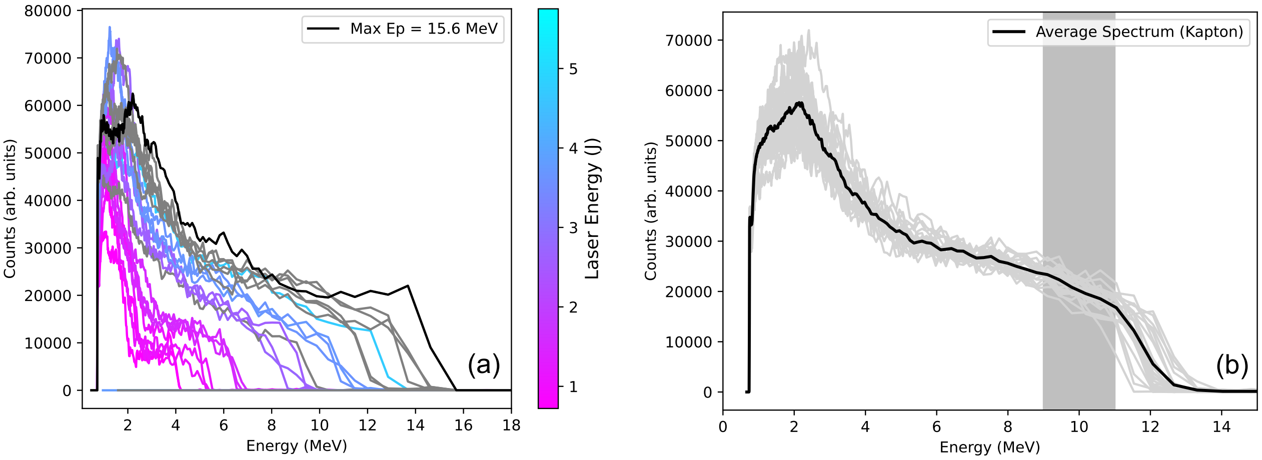

Figure 10: Proton spectra measured on TP spectrometer (a) Proton spectra measured for N=27 shots over an energy range of $E_L = 0.72 - 5.75$ J. (b) Proton spectra measured over N=23 repeat shots at maximum laser energy.

Alongside the beam spatial profile measurement, the proton energy spectrum was also measured with the RCF dosimetry stack. The recovered, calibrated spectrum is shown in figure 9(a-b). In (a) we show the spectrum and indicate, in the grey box, the region of spectra used for the calculations in section 2.5. The measured cut-off for the spectrum on this shot is $E_p = 13.9 \pm 1.3$ MeV. It should be noted that this measurement comes from a single laser pulse and the measurement, especially around the cut off, is subject to shot-to-shot variation. The integrated band around $E_p = 10 \pm 1$ MeV contains 7×10^9 protons. In order to validate this measurement of the proton spectrum we compare to previously published data from the J-KAREN laser system [5]. Here the laser energy is higher ($E_L = 10$ J), the target thinner ($L = 5\,\mu$m steel) and the encircled energy approximately a factor 2 higher. This combination of a thinner target and higher on target laser energy naturally leads to significantly higher maximum proton energies and higher total flux than measured on SCAPA. We can extrapolate our measured flux by scaling the spectrum by the factor 2 increase in encircled energy we would expect to achieve on future experiments, as outlined in section 2.1. This is shown as the orange line in (b), with an increase in proton numbers in the $E_p = 10 \pm 1$ band to 1.4×10^{10} protons. Without further optimisation of the target thickness (moving to thinner targets) or further control of the preplasma density profile, this is the likely highest proton flux achievable in this band with the current experimental arrangement. As a further check on this measurement we scale the flux by the ratio of the laser energy on SCAPA to that on J-KAREN and find that two measured spectra fall on the approximately the same line. This gives additional confidence that both this calibration and the experimental parameters on SCAPA are comparable with leading international systems.

Given the single-use, film based nature of the RCF dosimetry stack it is not possible to build up detailed data scans or a statistical understanding of the performance of the proton source using this approach. In figure 10 we show measurements made of the proton beam with the TP spectrometer [6]. In figure 10(a) we show the scaling of the proton spectrum accelerated from a steel tape ($L = 10\,\mu$m) over a series of shots (N = 27) where we vary the laser energy between $E_L = 0.72 - 5.75$ J. Here we observe a maximum proton energy of $E_p = 15.6$ MeV for the highest laser energy on target. Shots where the laser energy measurement was not available are shown as grey lines. It is also important to note that the TP spectrometer data is not in calibrated proton numbers at the present time and is reported instead as counts measured on the CCD camera (a new method is currently being developed to apply calibration data to this detector). The measured maximum proton energy is higher than seen on the RCF dosimetry stack, despite the fact that the TP spectrometer is further away from the target (≈ 1

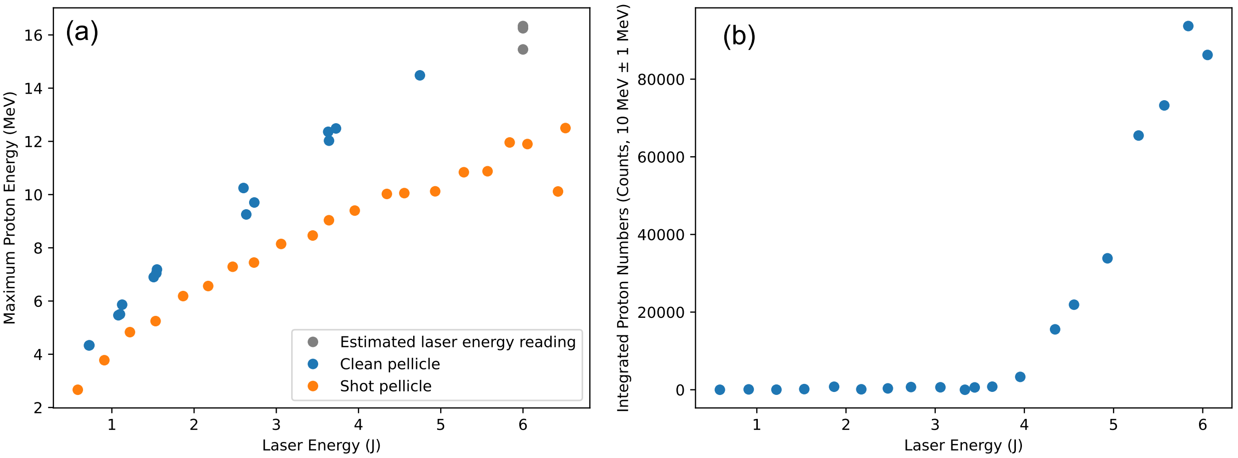

Figure 11: (a) Scaling of maximum proton energy as a function of laser energy. Showing the difference in performance of the source when a new pellicle is used compared to one which has accumulated hundreds of shots. (b) Scaling of the number of protons in a $E_p = 10 \pm 1$ MeV band as a function of laser energy.

m) than the RCF dosimetry stack and samples a considerably smaller solid angle (0.8 μSr compared to 4 Sr). The amplification provided by the micro-channel plate (MCP) detector used gives good sensitivity at the proton cutoff energy and given the capability to make repeat measurements, a greater chance to observe the highest cutoff energies as the laser energy slightly fluctuates. In figure 10(b) we show a series of direct repeat shots on a kapton tape (N=23) taken during a data scan to measure the stability of the proton spectrum measured with the TP spectrometer. Kapton was used during a series of stability scans given it produced significantly lower EMP which resulted in easier, higher repetition rate operation of the laser. The average maximum proton energy and standard deviation over these repeat shots is found to be $\overline{max(E_p)} = 12.9 \pm 0.5$ MeV. The average flux in the $E_p = 10 \pm 1$ MeV band is found to have a coefficient of variation (CV) of $\frac{\sigma_{10\pm1}}{\overline{N_{10\pm1}}} = 8.4\%$. This value is expressed here as the CV in percentage rather than the standard deviation in absolute terms given that the TP does not have a proton number calibration at the present time. The CV of the laser energy during the same data scan was only $\frac{\sigma_{E_L}}{\overline{E_L}} = 0.9\%$ and thus does not explain the variability seen in the integrated proton signal on its own (given our previously observed linear scaling). The source of this instability will be discussed in the next section.

In addition to measuring the change in the proton spectrum as the laser energy is varied (and its stability in direct repeat shots) it is important to also consider the scaling of the proton maximum energy and flux within the $E_p = 10 \pm 1$ MeV band as a function of laser energy. In figure 11(a) we show the scaling of the maximum proton energy measured on the TP as a function of laser energy. The points in blue are taken with a pellicle that had not previously been shot. The points in orange are using a pellicle that has accumulated hundreds of shots prior to making this measurement, as shown in in figure 4(b) this will effectively reduce the energy on target. The points shown in grey are at a setting where the laser is at full energy but where the on-shot energy measurement did not record a value, we estimate the laser energy in this case to be 6 J (which is justified given the stability shown in figure 4(a)). The most salient point about this data is that in order to reach the highest proton energies possible in this configuration, on target energy is the key parameter. This needs to be considered both in terms of the laser energy output but also the throughput of the compressor, the transmission of the pellicle and the encircled energy in the spot. The pellicle damage accumulated over hundreds of shots is worth significant consideration in the future. On the same data scan with the clean pellicle we can also measure the integrated proton signal in the $E_p = 10 \pm 1$ MeV band. Here we see that essentially we need more that 4 J on target to measure any protons around 10 MeV. Above this threshold value the flux in the band scales linearly with energy. This insight provides a clear motivation to optimise the energy on target in SCAPA for radiobiology experiments and also, in the design of the future ITRF facility, to consider designing in a significant pulse energy overhead in the laser.

In this section we have introduced a number of important measurements characterising the laser-driven proton source on SCAPA. We have demonstrated that we have been able to exceed the 15 MeV maximum proton energy that was targeted during this phase of the project. Analysis of the data from these first experiments show that optimising energy on target will be key and that minimising effects (such as loss of encircled energy in the spot or loss of transmission through the pellicle) will be key to maintaining a proton source parameters within the range needed for future radiobiology experiments.

2.4 Proton source stability

A final aspect of the measured proton source worth considering is its measured shot to shot stability. As shown in figure 10(b) the apparent CV in the $E_p = 10 \pm 1$ MeV band is found to be $\frac{\sigma_{10\pm1}}{N_{10\pm1}} = 8.4\%$ but this does not correspond to the much smaller measured variation in the laser energy. Here we investigate the potential sources of this variation. In figure 12 we show the distribution of the integrated proton signal in the $E_p = 10 \pm 1$ MeV band. Showing the variation in flux discussed previously. On this data scan a 2D beam profile monitor was inserted in the beam. This beam profiler consisted of an aluminum foil filter, a 700 μm mylar filter and a Lanex scintillator. This enabled on shot measurements of the spatial profile of the beam for $E_p \geq 8.4$ MeV. In figure (b) we compare the distribution of the integrated proton spectrum measured on the TP to the integrated signal measured on the footprint monitor. The signals are normalised to the maximum signal measured on each detector such that the relative variation in signal on the same shots for the two different detectors becomes clear. Here we see that the variation measured on the TP spectrometer is significantly higher than that measured on the footprint monitor. Applying the same CV measurement as before to the signal on the we find that $\frac{\sigma}{N} = 2\%$ which is significantly closer to the 1% CV measured for the laser energy. It likely therefore that the variation seen in the proton signal as measured on the TP spectrometer is in fact not as a result of genuine shot-to-shot variation in the proton flux but for another reason. In order to investigate this further we measured the centroid of the beam profile on the footprint monitor over the shots within this data scan. The coordinates of the centroid in X and Y-directions is shown in (c) with the radial distance shown on the colourbar. This data indicates that there is approximately 175 μm and 300 μm variation of the proton beam in the Y- and X-direction, respectively. The beam profile is measured at 4.5 cm behind the target and thus we would not expect the same magnitude of variation as seen on the focal-spot jitter measurements in absolute terms. It is interesting to note however that despite the large asymmetry seen in the focal-spot jitter (dominated by the Y-motion), this is not reproduced here.

The key insight from this data is that although a shot-to-shot variation of around 10% (CV) in proton flux was measured on the TP spectrometer in the $E_p = 10 \pm 1$ MeV band, the shot-to-shot variation measured from the footprint monitor is much smaller at around 2%. This indicates the that variation in the performance of the source is small and on the percent level equivalent to the variation in the laser energy. This is a strong positive for the stability of delivered dose on future radiobiology experiments. The observed variation is in-fact a result of the small solid angle of the beam that is measured by the TP spectrometer and the measured spatial jitter of the proton beam pointing. Further development work will focus on reducing the laser focal-spot spatial jitter to help reduce the pointing jitter of the proton beam, this will have a two-fold effect of improving the measurement of the proton spectrum and aiding in the performance of the proposed proton capture beamline.

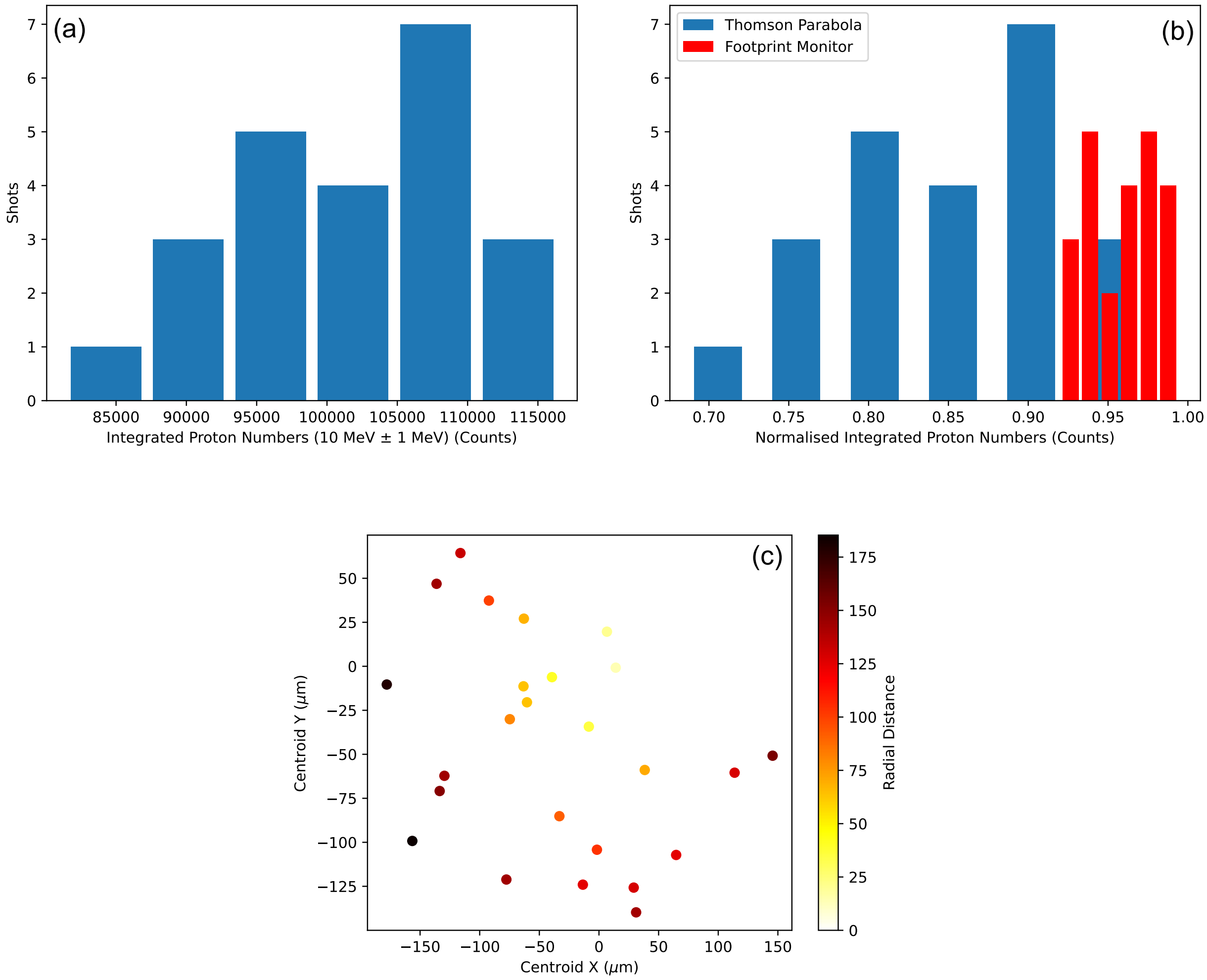

Figure 12: (a) Distribution of proton flux measured in a band $E_p = 10 \pm 1$ MeV over N=23 shots. (b) Distribution of flux measured in a band $E_p = 10 \pm 1$ MeV over N=23 shots normalised to maximum flux for both the TP spectrometer and footprint monitor. (c) Centroid of the proton beam profile measured on footprint monitor for N=23 shots in X- and Y- dimensions. The radial displacement is shown on the colourbar.

2.5 Proton source performance for future radiobiology experiments

It is important to consider what the measured parameters of the proton source on the first SCAPA experiments means for the first radiobiology experiments in the next phase of the project. If we take the $E_p = 10 \pm 1$ MeV band previously extracted from the proton spectrum measured on the RCF dosimetry stack in figure 9(a) where the number of protons was $N_p = 7 \times 10^9$. Assuming the density of the medium the protons stop in is equivalent to water, the protons would have an average range of $R_p = 1.2$ mm. If we conservatively estimate that any capture beamline has 5% transmission for protons of this energy and the size of the beam at the point of irradiation is $r = 1$ cm then total dose per shot is calculated to be $D_{10\pm1} = 0.91$ Gy/shot. For the range of energies considered we can calculate the time of flight spreading of a 1 m beam path, assuming the initial duration of the proton bunch is equal to the laser pulse duration. Over this distance the proton pulse is found to spread out to $t_p = 2.34$ ns. We can then calculate the peak dose rate on a given shot to be $dD_{10\pm1}/dt = 3.1 \times 10^8$ Gy/s. Given the pulsed nature of the source and a repetition rate of 0.3 Hz, the average dose rate per minute is $dD_{10\pm1}/dt = 16$ Gy/min. The instantaneous dose rate measured to date therefore substantially exceeds the dose rates needed for FLASH. However it remains to be seen if the total dose also needs to increase in order to see biologically relevant effects. Based on the discussion in earlier sections of the report regarding planned work to increase the repetition rate up to 1 Hz and to double the effective energy on target it is possible to considerable increase these calculated doses. It may also be possible to optimise the beamline for up to 10% transmission. Using these updated values the dose per shot becomes $D_{10\pm1} = 3.62$ Gy/shot, the peak dose rate becomes $dD_{10\pm1}/dt = 1.25 \times 10^9$ Gy/s and the average dose rate becomes $dD_{10\pm1}/dt = 217.4$ Gy/min. These inputs are achievable in the next phase of the project and would significantly exceed the dose rates needed for FLASH radiobiology work.

3 Simulations

In this section, we will introduce recent work on realistic multi-scale simulations which combine outputs from both hydrodynamic and particle-in-cell codes. This multi-scale approach enables us to appropriately model the front surface plasma expansion induced by the laser temporal intensity contrast. Aspects of the initial development of these simulations were detailed in milestone report 2.1, here we extend the simulations to accurately include values measured on SCAPA as inputs to the simulations.

3.1 Summary of previous milestone report

The previous milestone report (M2.1) details a comprehensive series of high-fidelity hydrodynamic and kinetic (particle-in-cell or PIC) simulations carried out to predict a set of optimised proton source parameters for 300+ TW laser systems. The report describes the impact of several laser and target parameters on the acceleration of protons and carbon ions via TNSA from a solid aluminium target. The simulation previously reported predicted lower or upper thresholds for the source parameters that will ensure the acceleration of protons with the energy and flux required for LhARA. In the presence of optimal laser contrast and sharp plasma-to-vacuum transition, very thin targets ($<2\,\mu\mathrm{m}$) and laser intensities $\gg 10^{21}\ \mathrm{W/cm^2}$ were found to be required to extend the proton spectrum beyond $20\,\mathrm{MeV}$ and accelerate sufficient protons to energies of $(15.0 \pm 0.5)\,\mathrm{MeV}$.

In addition, the previous milestone report highlighted the proper modelling of the laser contrast and density profile of the target as important factors which play a significant role in obtaining realistic energy spectra of the protons accelerated via TNSA. Our results showed that a preplasma with a several-micrometres-long scale length and near-critical density can strongly enhance proton acceleration even with the use of not-so-thin

Table 1: Summary table of the main parameters used to model the TNSA mechanism for proton acceleration under similar conditions to the most recent experiments at SCAPA [7].

	Parameter	**Value**	**Unit**
Laser	Energy (in the laser spot)	1.32	J
(p-polarised)	Pulse duration	25	fs
	Intensity (I_0)	1.4×10^{21}	$\mathrm{W/cm^3}$
	Spot size† (w_0)	1.5	µm
	Angle of incidence	35	°
	Laser pulse rise/fall time	25.06	fs
	Wavelength (λ_0)	800	nm
	Norm. laser vector potential (a_0)	25.63	
	Critical density (n_c)	1.74×10^{21}	$1/\mathrm{cm}^3$
Target	Thickness	10	µm
(Fe^{3+})	Density	200	n_c
	H$^+$ layer thickness	31.83	nm
	H$^+$ layer density	1.15	n_c
	Initial particle temperature	10	keV

† w_0 is the pulse waist ($= \mathrm{FWHM}/\sqrt{2\ln 2}$)

tape targets. In a scenario when the highest available laser intensity is used in combination with the thinnest target that can be run on the tape-drive system, controlling the preplasma represents one of the few remaining approaches to further increase the maximum achievable energy and the number of protons accelerated from the target. Thus, a key outcome of the previous milestone report was the importance of developing new methods to measure and control the preplasma for solid targets that can be run at high repetition rates for creating optimal conditions for proton and ion acceleration from solid targets via TNSA.

Following the previous milestone report, some of the parameters of the PIC model of the laser and the tape target have been updated to better match the experimental conditions at SCAPA. Firstly, the laser pulse energy and the target thickness have both been increased from approximately $1\,\mathrm{J}$ to $1.3\,\mathrm{J}$ and from $6\,\mu\mathrm{m}$ to $10\,\mu\mathrm{m}$, respectively. Secondly, the composition of the target has been changed to Fe ions since the highest proton energies have been obtained on SCAPA with steel tape targets. For the preliminary 2-D simulation outlined in this report, the maximum density of the target has been increased to $200\,\mathrm{n_c}$ from the value of $70\,\mathrm{n_c}$ used previously for the Al target in 3-D simulations. The updated set of parameters of the PIC model is summarised in Table 1.

3.2 Realistic multi-scale simulations (hydrodynamic + PIC)

The most recent measurement of the laser contrast (July 2024, see figure 7) was used as an input to a new set of hydrodynamic simulations using the FLASH code [8]. The previous campaign of PIC simulations considered an aluminium target as the baseline model. Nonetheless, the highest proton energies have been measured on SCAPA from steel tape targets. The expansion of the preplasma before the arrival of the main laser pulse is influenced by the ion species in the target and the ionisation levels induced by the laser. Hence, it is important to evaluate any potential differences between the preplasma expansion profiles in the cases of aluminium and steel targets to draw valid comparisons between the results of the PIC simulations and the measurements at SCAPA. The new set of simulations in FLASH considered more realistic density and equation-of-state data closer to those of iron (Fe). The code was run in 2D cylindrical geometry and models the prepulse absorption with an inverse bremsstrahlung heating model based on ray tracing. Heat conduction and exchange between electrons and ions are based on the Lee-More model.

Figure 13(a) shows the expansion of the target material on the front surface of the Fe target $5\,\mathrm{ps}$ before the arrival of the main laser pulse. The resulting preplasma profile does not exhibit spherical symmetry around the point where the laser is focused on the target. As a general property, the prepulse-driven ablation plasma has two scale lengths. This is due to the heating characteristics of the laser. The heating rate for inverse bremsstrahlung increases exponentially as the ionised electron density reaches the plasma critical density. Therefore, most of the absorption happens in a relatively confined region around the plasma critical density. The longer scale length, ion density below approximately $1\,\mathrm{n_c}$ in figure 13(b), is the ablation plasma. This is matter that has been driven away from the front surface due to the thermal pressure generated at the critical density surface. The shorter scale length, just in front of the bulk of the target, is the conduction layer. Here, plasma heating is dominated by heat conduction into the target from the critical density surface.

To use the preplasma density profile obtained with the FLASH code, the electron density along the direction of incidence of the laser was fitted with a piece-wise linear function. The algebraic expression of the best-fit function was subsequently used to set up the starting target density profile in the PIC simulation. Figure 13(b) indicates two pairs of scale lengths, one for the ablation plasma and one for the conduction layer. Since the maximum target density is limited in PIC simulations by numerical heating, a cutoff density of $200\,\mathrm{n_c}$ was chosen for the bulk of the target.

Figure 14 shows a comparison between the resulting ion expansion profiles on the front surface of the target for aluminium or iron as the material of the target. The aluminium target expands more into the vacuum and exhibits a longer length scale for the ablation region. In the conduction layer, both target materials show similar plasma expansion profiles. The longer length scales observed in the case of an aluminium target may result in a longer region of electrons in the preplasma close to the critical density and, in turn, to larger proton cutoff energies compared to the case of an iron target.

The 2-D PIC simulations were performed using OSIRIS [9] on the HPC cluster ARCHER2 [10]. A box of $360 \times 310\ \mathrm{\mu m}$ was simulated with spatial resolution $16 \times 16\ \mathrm{nm}$. The target was composed of $10\,\mathrm{\mu m}$ preionised iron at 35° angle of incidence, with 64(16, 144) particles per cell for electrons(Fe ions, H ions). To minimize numerical heating, the peak target electron density was restricted to $200\,\mathrm{n_c}$, still significantly higher than $\mathsf{n_c}$. The preplasma density profile was initialised from the results of the hydrodynamic simulation using the piece-wise linear function shown in figure 13(b). The density profile obtained from the hydrodynamic simulation was translated into the PIC model by assuming full ionisation of the Fe ions.

3.2.1 Results of hydrodynamic + PIC

Figure 15 summarises the results of a 2-D PIC simulation for which we considered an oblique $10\,\mathrm{\mu m}$-thick Fe target rotated at 35° with respect to the direction of incidence of a laser pulse with intensity $I_0 = 1.4 \times 10^{21}\,\mathrm{W/cm^2}$ ($a_0 = 25.63$). Under these conditions and in combination with the model of the more realistic preplasma based on a separate hydrodynamic simulation and the most recent laser contrast curve measured at SCAPA, we notice that the proton cutoff energy is $\simeq 18\,\mathrm{MeV}$ at the last time step of the simulation. The full energy spectrum of the protons accelerated from the target is shown in figure 15(b).

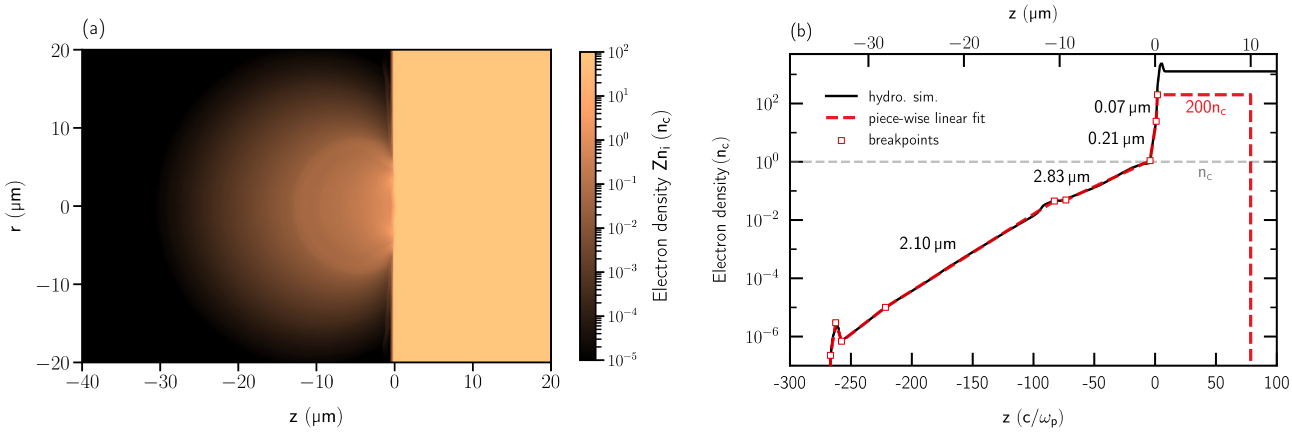

Figure 13: (a) Predicted maximum electron density on the front surface of a Fe target 5 ps before the arrival of the main laser pulse extracted from a 2-D hydrodynamic simulation using the FLASH code. The laser is incident at 35° onto the target and was modelled based on the most recent contrast curve measured at SCAPA (July 2024, figure 7). (b) Lineout of the maximum electron density (black) along the laser axis of propagation fitted with a piece-wise linear function (red). The initial target front surface was at $z = 0\,\mu\mathrm{m}$. The density of the bulk of the target is cut off at $200\,\mathrm{n_c}$. Four length scales are shown for the main regions of the preplasma.

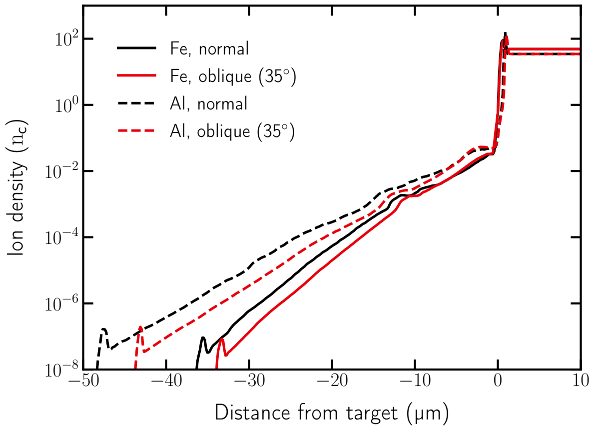

Figure 14: Ion density profiles predicted by the FLASH code on the front surface of a tape target along the normal to the target and the direction of incidence of the laser (35°). An iron and an aluminium target were considered separately. A typical double exponential scale is formed during the prepulse-driven ablation. The initial target front surface was at $0\,\mu\mathrm{m}$.

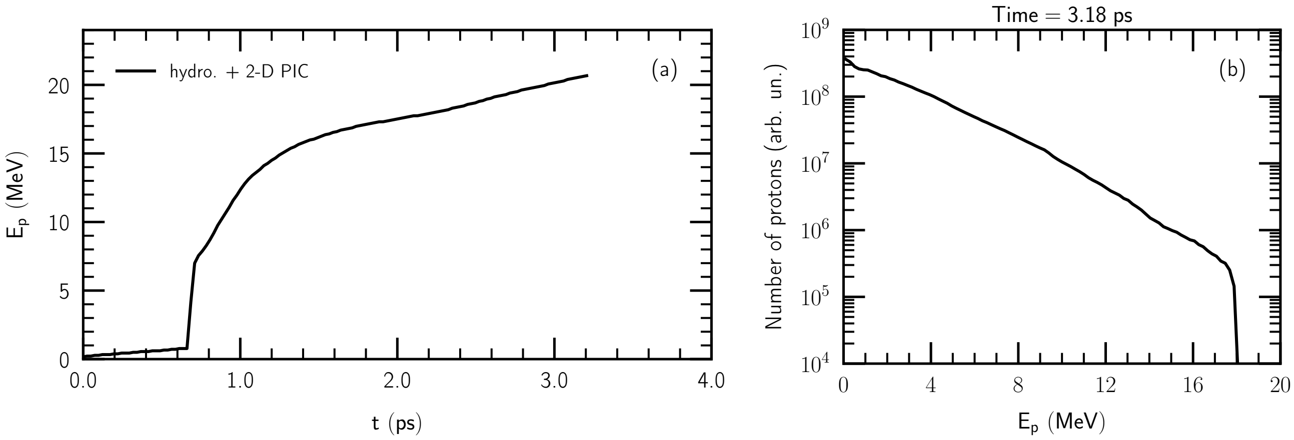

Figure 15: (a) Evolution of the maximum proton energy. (b) Proton energy spectrum at the last time step of the simulation. The 2-D PIC simulation considered a laser with intensity $1.4 \times 10^{21}\,\mathrm{W/cm^2}$ incident at $35°$ on a $10\,\mu\mathrm{m}$-thick Fe target. The front surface of the target was pre-expanded according to the prediction of a separate hydrodynamic simulation (see figure 13).

3.3 Discussion of results in comparison to experiment

Figure 15(a) shows that in the 2-D simulations, the acceleration process is still ongoing even after 3 ps. In a 2-D simulation, the "point" charges effectively behave as infinite wires with finite linear charge density. On longer time scales the problem is nearly purely electrostatic and the logarithmic behaviour of the potential leads to a much slower "saturation" of the acceleration process and higher proton energies than those predicted by the equivalent 3-D simulation.

In the milestone M2.1 report on simulations of the LhARA source, we found that under similar preplasma conditions, the 2-D simulations overestimate the proton energies by a factor of approximately 1.6. Thus, the preliminary simulation reported here which made use of experimental measurements of key laser and target properties carried out on SCAPA predicts a lower bound for the proton cutoff energy of approximately $11\,\mathrm{MeV}$. This estimation remains to be verified by 3-D simulations. Nonetheless, the proton energy cut-off measured on SCAPA for specific laser shots ($E_p = 13.9 \pm 1.3$ MeV) exceeds the prediction of the 2-D PIC simulation. In addition, the measurements performed on SCAPA confirmed the predictions of the parameters scans carried out with PIC simulations and described in the milestone M2.1 report which predicted that the optimal source performance is found for the highest laser energy, shortest pulse, and smallest focal point.

3.4 Limitations

High-fidelity 3-D PIC simulations are well-known to require large computational resources. The total number of CPU hours required to run a 3-D simulation until the accelerated ions reach energy saturation increases even more under the following conditions: target thickness greater than approximately $5\,\mu\mathrm{m}$, angle of incidence of the laser of $30°$ or more, the presence of a preplasma in a region of several tens of $\mu\mathrm{m}$ in front of the target. Nonetheless, full-scale 3-D simulations are required to quantitatively predict the cutoff energy of the ions accelerated from the target and their energy spectrum. To identify scaling laws or optimise the laser and target parameters, the 2-D PIC simulations are suitable and more computationally affordable.

One limitation of the simulation model is the presence of an upper limit of the peak target electron density which is restricted by numerical heating. Even though we use a maximum electron density significantly higher than the critical density, the magnitude is well below the physical density of tape targets. In addition, an assumption has to be made regarding the ionisation level of the ions in the preplasma and the target when translating the density profiles obtained from the hydrodynamic simulation into the PIC model. For higher Z materials, the preplasma is likely to not be fully ionised for lower laser intensities. In the model presented here, the ionisation state of the ions in the preplasma was chosen so that the transition point between the conduction layer and ablated plasma comes close to the critical density as obtained at the end of the hydrodynamic simulation.

3.5 Future work on simulations

To build on this existing simulation work, a potential next step would be to carry out a full-scale PIC simulation in three dimensions with the realistic target and laser parameters modelled in the preliminary 2-D simulation reported above. Such a simulation is needed to further validate the PIC model against the measurements carried out on SCAPA. The 3-D model needs to include the prediction of the preplasma density profile from the separate hydrodynamic modelling of the target expansion and make use of the most recent experimental measurements of key laser and target properties from SCAPA. Given the greater thickness and density of the steel tape target used at SCAPA in comparison to the aluminium targets considered before in the PIC models, in addition to the angle of incidence of the laser, a prior evaluation is needed of the computational resources required to run such a full-scale realistic 3-D PIC simulation.

Secondly, given the relatively close agreement between simulation and experiment, the combination of hydrodynamic and PIC simulations is likely to be an important aid in optimising the source in the future. Previously, the parameter scans and optimisation runs were carried out using PIC simulations. The work described in the milestone M2.1 report indicated the main characteristics of an optimal preplasma profile that can enhance the proton cutoff energy as an alternative to increasing the laser energy or using thinner targets. Nonetheless, from the point of view of optimising the LhARA source, it is currently not well understood which target conditions or laser pre-pulse configurations are needed to produce an optimal preplasma at the front of the target. Hence, a detailed set of hydrodynamic parameter scans or optimisation studies, such as using Bayesian optimisation, are needed to show how the optimal prepalsma profile predicted by PIC simulations can be reproduced experimentally. The next steps could also include the application of Bayesian optimisation of both the hydrodynamic and PIC simulations simultaneously.

4 Summary

In summary, through a series of experiments conducted between July 2023 and July 2024 we have been able to deliver the first proton beam optimisation studies relevant for LhARA at SCAPA. In this effort we have identified key parameters related to the SCAPA laser performance including the on-shot laser energy and how this evolves in a high-repetition rate scenario as the pellicle accumulates damage and debris. In addition, we successfully removed prepulses present in the system which were detrimental to proton acceleration. In doing so we have demonstrated a source with a maximum proton energy $E_p = 15.6$ MeV with a measured proton number in the $E_p = 10 \pm 1$ MeV band of $N_p = 7 \times 10^9$. Through simple modelling of a potential radiobiology experiment we show that the proton source in its current configuration is capable of delivering FLASH relevant doses and dose rates. We also identify a number of potential areas to explore in the next phase of the project to increase these values further. The best route to optimising the source in the next phase is likely to be through optimisation of the encircled energy in the laser focal spot, in the transmission through the protective pellicle and in tuning of the preplasma density profile.

In addition to these measurements of the proton energy and flux we identify challenges in the proton beam pointing which likely related to jitter in the laser pointing. This variability results in a variability in the measured proton spectrum, we show this is likely due to the limited solid angle over which this measurement is made and not an underlying variability in the source.

In support of this effort to optimise the proton source we have developed new methodologies both in the laboratory and through numerical simulations. We have adapted the tape target system to be suitable for our geometry and developed new rapid data analysis and control systems for high repetition rate operations. These developments will prove critical in enabling statistical and data driven optimisation in the next phase. In simulations we have combined modelling in the hydrodynamic code FLASH with the particle-in-cell code OSIRIS and included experimentally measured parameters to perform realistic multi-scale modelling. The results from this modelling show good agreement with experimentally measured values and will form an important part of the experimental design in next phase.

From the data presented here, the source development effort in Work Package 1.2 is well placed to support delivery of internationally leading radiobiology experiments with laser-driven protons in the next phase of the project.

Acknowledgments

We gratefully acknowledge contributions from the experimental team on SCAPA bunker B including: B. Torrance, C. McQueen, M. Peat, M. Alderton, E. Dolier (University of Strathclyde), O. Etlinger, G. Casati (Imperial College London) and P. Parsons (Queens University Belfast). We also acknowledge the support of the SCAPA facility team S.M Wiggins, G. Manahan, E. Brunetti as well as target and equipment support from the Central Laser Facility.

References

[1] H. Kiriyama, Y. Miyasaka, A. Kon, *et al.*, "Enhancement of pre-pulse and picosecond pedestal contrast of the petawatt J-KAREN-P laser," *High Power Laser Science and Engineering* **9** (2021) e62.

[2] V. Schanz, F. Wagner, M. Roth, and V. Bagnoud, "Noise reduction in third order cross-correlation by angle optimization of the interacting beams," *Optics express* **25** (2017), no. 8, 9252–9261.

[3] E. Clark, K. Krushelnick, M. Zepf, *et al.*, "Energetic heavy-ion and proton generation from ultraintense laser-plasma interactions with solids," *Physical Review Letters* **85** (2000), no. 8, 1654.

[4] F. Nürnberg, M. Schollmeier, E. Brambrink, *et al.*, "Radiochromic film imaging spectroscopy of laser-accelerated proton beams," *Review of scientific instruments* **80** (2009), no. 3,.

[5] N. Dover, M. Nishiuchi, H. Sakaki, *et al.*, "Demonstration of repetitive energetic proton generation by ultra-intense laser interaction with a tape target," *High Energy Density Physics* **37** (2020) 100847.

[6] D. Carroll, P. Brummitt, D. Neely, *et al.*, "A modified Thomson parabola spectrometer for high resolution multi-MeV ion measurements—Application to laser-driven ion acceleration," *Nuclear Instruments and Methods in Physics Research Section A: Accelerators, Spectrometers, Detectors and Associated Equipment* **620** (2010), no. 1, 23–27.

[7] S. M. Wiggins, M. Boyd, E. Brunetti, *et al.*, "Application programmes at the Scottish Centre for the Application of Plasma-based Accelerators (SCAPA)," in *Relativistic Plasma Waves and Particle Beams as Coherent and Incoherent Radiation Sources III*, D. A. Jaroszynski and M. Hur, eds., vol. 11036, p. 110360T, International Society for Optics and Photonics. SPIE, 2019. doi:10.1117/12.2520717.

[8] B. Fryxell, K. Olson, and P. Ricker, "FLASH: An Adaptive Mesh Hydrodynamics Code for Modeling Astrophysical Thermonuclear Flashes," *The Astrophysical Journal Supplement Series* **131** (2000) 273–334, doi:10.1086/317361.

[9] R. A. Fonseca, L. O. Silva, F. S. Tsung, *et al.*, "OSIRIS: A Three-Dimensional, Fully Relativistic Particle in Cell Code for Modeling Plasma Based Accelerators," in *Computational Science — ICCS 2002*, P. M. A. Sloot, A. G. Hoekstra, C. J. K. Tan, and J. J. Dongarra, eds., pp. 342–351. Springer Berlin Heidelberg, Berlin, Heidelberg, 2002. doi:10.1007/3-540-47789-6_36.

[10] ARCHER2–UK National Supercomputing Service. `https://www.archer2.ac.uk/`, 2024. Accessed: May 2024.